Decoupled Current Control Using Adaptive Quasi Resonant-Based ESO for Novel Matrix-Torque-Component Machines

Shaofeng Jia, *Senior Member, IEEE*, Dongxu Yang, *Student Member, IEEE*,
Pengcheng Sun, *Student Member, IEEE*, Deliang Liang, *Senior Member, IEEE*, and Jikai Si, *Member, IEEE*

***Abstract*—This article proposes a current loop decoupling control method tailored for a novel matrix-torque-component machine (MTCM). The proposed decoupling controller is based on an adaptive quasi resonant extended state observer (AQRESO). A distinctive feature of the MTCM is its arrangement of windings and permanent magnets on both the stator and rotor. The coupling term in the MTCM current loop originates from two primary sources: one being the dc disturbance, which is proportional to the stator-rotor mutual inductance, and the other being the ac disturbance, caused by current harmonics due to nonlinear factors. The proposed AQRESO integrates a quasi-resonant controller in parallel with the traditional linear extended state observer (LESO), enabling the observation and compensation of both ac and dc disturbances. Meanwhile, the ESO gain is adaptively regulated according to the current error to avoid the decrease in noise suppression ability caused by excessive gain. The stability and harmonic suppression performance of the proposed controller have been rigorously analyzed. Finally, the effectiveness of the proposed method is validated experimentally on an MTCM prototype.**

***Index Terms*—Adaptive gain, decoupling control, matrix torque component, quasi resonant linear extended state observer (LESO).**

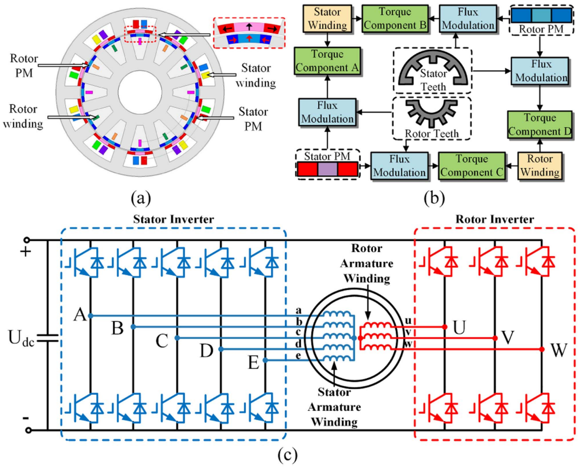

Fig. 1. (a) Topology of the stator 5-phase, 10-slot, rotor 3-phase, and 12-slot novel MTCM. (b) Matrix torque component generation principle. (c) Topology of the MTCM drive circuit.

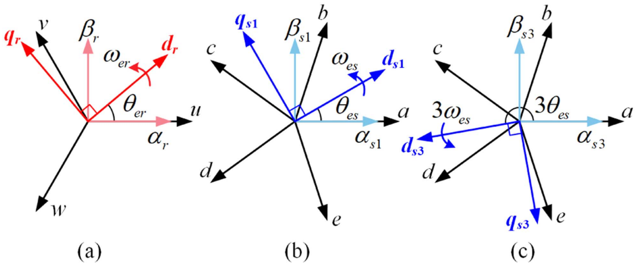

Fig. 2. Schematic of the double rotating reference frame. (a) Rotor d_r-q_r frame. (b) d_{s1}-q_{s1} frame of the stator fundamental space. (c) Stator d_{s3}-q_{s3} frame of the stator third harmonic space.

I. INTRODUCTION

HIGH torque density permanent magnet synchronous machines (PMSMs) used in electric vehicles (EVs), electric actuator systems, ship propulsion [1], [2], [3], and so on are gaining much attention in recent years. Researchers have proposed several innovative PMSM topologies with multiple magnetic sources based on the flux modulation principle to meet the growing demand for higher torque density. For instance, a novel doubly-fed flux reversal machine enhances torque density by adding windings on the rotor side [4]. Dual-side permanent magnet machines utilize permanent magnets (PMs) on both stator and rotor, thereby achieving higher torque density through bidirectional flux modulation [5].

To further improve torque density, a novel dual-winding dual-magnet machine has been investigated in [6] and [7]. This machine incorporates armature windings and PMs on both the

Received 28 August 2024; revised 11 December 2024; accepted 20 January 2025. Date of publication 30 January 2025; date of current version 20 March 2025. This work was supported in part by the National Natural Science Foundation of China under Project 52277066 and in part by the State Key Laboratory of Electrical Insulation and Power Equipment Foundation under Grant EIPE23131. Recommended for publication by Associate Editor K. Lee. *(Corresponding author: Shaofeng Jia.)*

Shaofeng Jia, Dongxu Yang, Pengcheng Sun, and Deliang Liang are with the State Key Laboratory of Electrical Insulation and Power Equipment, School of Electrical Engineering, Xi'an Jiaotong University, Xi'an 710049, China (e-mail: shaofengjia@xjtu.edu.cn; dongxuyang@stu.xjtu.edu.cn; sunpengcheng123@stu.xjtu.edu.cn; dlliang@xjtu.edu.cn).

Jikai Si is with the School of Electrical and Information Engineering, Zhengzhou University, Zhengzhou 450001, China (e-mail: sijikai@zzu.edu.cn).

Color versions of one or more figures in this article are available at https://doi.org/10.1109/TPEL.2025.3534325.

Digital Object Identifier 10.1109/TPEL.2025.3534325

stator and rotor sides. Leveraging a special slot-pole combination, the machine can simultaneously output multiple torque components in a matrix arrangement, thereby further enhancing output torque. Consequently, this new type of machine is also referred to as a matrix-torque-component machine (MTCM). The topology and matrix torque generation principle are depicted in Fig. 1(a) and (b). The stator and rotor windings interact with the stator and rotor PMs, respectively, to produce four torque components. The topology of the MTCM drive circuit is illustrated in Fig. 1(c). The stator of the MTCM is powered by a five-phase full-bridge inverter, and the rotor is powered by a three-phase full-bridge inverter. The two inverters have a common dc-bus, so the power supply topology can also be called an eight-phase common dc-bus inverter. The corresponding three-phase inverter supplies power to the rotor winding via slip rings and brushes.

Sun et al. [6] has proved that under the same copper loss and same size, the torque density of the MTCM is 63% higher than that of the surface-mounted PMSM, while the amount of PM is only 17% higher than that of the latter. Although the rotor needs to be powered by brushes and slip rings, with the development of brush materials [8], [9], the life and reliability of brushes and slip rings are also continuously improved. Based on the advantages, the MTCM has the potential to be used as the drive machine of EVs or actuator machine.

To fully leverage the advantages of matrix torque components, precise current loop control is essential. However, the current loop coupling of the MTCM is more complex than that of traditional PMSMs. This is attributable to two primary factors. First, the mutual inductance between the stator and rotor windings results in the voltage equation containing complex coupling terms, which can be further exacerbated by parameter mismatches. Second, the special winding configuration and nonlinear factors lead to significant harmonics in the phase current. The components of these harmonics on the *d–q* axes result in periodic ac coupling. Due to these factors, the traditional feedforward decoupling method cannot effectively address the current loop coupling problem in the MTCM. However, recent literatures focus more on the fault-tolerant control of MTCM or novel machines based on similar principles [10], [11], the research on MTCM current loop decoupling control and harmonic suppression is still blank.

The disturbance estimation and attenuation technique is an effective approach to solve the current loop coupling issue [12], [13]. It regards the coupling terms as disturbances, estimates and compensates them through observers. Among the existing observers, the extended state observer (ESO) demonstrates robust anti-disturbance performance and model-free characteristics. To address the complexity in parameter design of the ESO, linear ESO (LESO) was proposed in [14] and has been widely used in disturbance control [15]. However, the traditional LESO acts more like a low-pass filter for disturbance estimation, thus only effectively suppressing the dc disturbance [16]. As previously mentioned, the MTCM current loop contains not only dc disturbances but also ac disturbances caused by harmonics. The ac disturbances can cause *dq*-axes current ripples, deteriorating the dynamic- and steady-state performance [17]. To simultaneously suppress the dc and ac disturbances, improved ESOs based on resonant controllers [18], [19], complex coefficient filters [20], quasi-resonant controllers [21], [22], and generalized integrators [23] have been presented in recent years. These improved ESO methods can be summarized as estimating the ac disturbance at the resonant frequency through a class of resonant controllers. Since the bandwidth of the quasi-resonant controller around the resonant frequency is improved compared to the ideal resonant controller, the quasi-resonant ESO (QRESO) has a better ability to deal with frequency deviations compared to other improved ESOs. As an improved LESO, QRESO requires large ESO gains to achieve rapid convergence. However, excessive gain increases the sensitivity of the ESO to noise, thereby deteriorating the controller's performance. Notably, existing research on QRESO has not adequately addressed this issue.

To suppress both dc and ac disturbances in the MTCM current loop while addressing noise sensitivity, this paper proposes an improved QRESO with adaptive gains. This scheme effectively decouples the MTCM current loop and guarantees the accurate output of matrix torque. The main contributions of this article are as follows.

1) This article first theoretically analyzes the coupling in the MTCM current loop, providing expressions for the dc and ac coupling disturbance terms. A current loop model of the MTCM that accounts for these coupling terms is established.
2) An adaptive QRESO is constructed to estimate both dc and ac disturbances in the MTCM current loop. By compensating the total disturbances, the current loop is decoupled, improving transient and steady-state performance.

The rest of this article is organized as follows. The mathematical model and matrix torque expression of the MTCM is constructed in Section II. Current loop model considering dc and ac coupling are analyzed in Section III. In Section IV, adaptive QRESO and its characteristic are investigated. Section V gives the stability analysis of the proposed method. Experimental results are shown in Section VI. Finally, Section VII concludes this article.

II. MATHEMATICAL MODEL OF THE MTCM

The mathematical model of the stator five-phase, rotor three-phase MTCM illustrated in Fig. 1 under the dual-rotating *d–q* reference frame is derived in this section.

The dual-rotating reference frame contains the rotor d_r-q_r frame and the stator d_{s1}-q_{s1}-d_{s3}-q_{s3} frame, which are illustrated in Fig. 2. The components in the d_{s3}-q_{s3} axis are mapped in the third harmonic space of the five-phase stator. ω_{es} and ω_{er} are the electrical angular frequency of the stator and rotor. θ_{es} and θ_{er} are the electrical angle of the stator and rotor. In the stator third harmonic space frame shown in Fig. 2(c), $3\omega_{es}$ represents the electrical frequency of the d_{s3}-q_{s3} axis system.

The relationship between the electrical angle, electrical angular frequency and mechanical angular frequency of the MTCM is satisfied as follows:

$$\begin{cases}\theta_{es} = \omega_{es} t = p_{ns}\omega_m t \\ \theta_{er} = \omega_{er} t = p_{nr}\omega_m t\end{cases} \tag{1}$$

where p_{ns} and p_{nr} are the pole pair number corresponding to the stator and rotor electrical angular velocity, respectively. ω_{es} and ω_{er} are the electrical angular velocity of the stator and rotor. ω_m is the mechanical angular velocity. Note that according to the principle of flux modulation, p_{ns} is equal to the number of rotor slots, and vice versa. Detail finds in [6].

The transformation matrix can be expressed by

$$\mathbf{T} = \begin{bmatrix} \mathbf{T_s} & \mathbf{0_{5,3}} \\ \mathbf{0_{3,5}} & \mathbf{T_r} \end{bmatrix} \tag{2}$$

where $\mathbf{T_s}$ and $\mathbf{T_r}$ are same with the transformation matrices of the conventional five-phase and three-phase PMSMs.

Neglecting the zero-sequence component equations, the voltage equation in dual rotating reference frame can be expressed as follows:

$$\boldsymbol{u} = \boldsymbol{R}\boldsymbol{i} + \frac{d\boldsymbol{\psi}}{dt} + \boldsymbol{\omega}\boldsymbol{\psi}. \tag{3}$$

Equation (3) can be further expanded as

$$\begin{bmatrix} u_{ds1} \\ u_{qs1} \\ u_{ds3} \\ u_{qs3} \\ \hdashline u_{dr} \\ u_{qr} \end{bmatrix} = \left[\begin{array}{cccc:cc} L_{ds1} & 0 & 0 & 0 & 1.5M_{sr} & 0 \\ 0 & L_{qs1} & 0 & 0 & 0 & 1.5M_{sr} \\ 0 & 0 & L_{ds3} & 0 & 0 & 0 \\ 0 & 0 & 0 & L_{qs3} & 0 & 0 \\ \hdashline 2.5M_{sr} & 0 & 0 & 0 & L_{dr} & 0 \\ 0 & 2.5M_{sr} & 0 & 0 & 0 & L_{qr} \end{array}\right] \cdot \frac{d}{dt} \begin{bmatrix} i_{ds1} \\ i_{qs1} \\ i_{ds3} \\ i_{qs3} \\ \hdashline i_{dr} \\ i_{qr} \end{bmatrix} + \begin{bmatrix} R_s i_{ds1} \\ R_s i_{qs1} \\ R_s i_{ds3} \\ R_s i_{qs3} \\ \hdashline R_r i_{dr} \\ R_r i_{qr} \end{bmatrix} + \begin{bmatrix} -\omega_{es}(L_{qs1} i_{qs1} + 1.5M_{sr} i_{qr}) \\ \omega_{es}(L_{ds1} i_{ds1} + 1.5M_{sr} i_{dr}) \\ -3\omega_{es} L_{qs3} i_{qs3} \\ 3\omega_{es} L_{ds3} i_{ds3} \\ \hdashline -\omega_{er}(L_{qr} i_{qr} + 2.5M_{sr} i_{qs1}) \\ \omega_{er}(L_{dr} i_{dr} + 2.5M_{sr} i_{ds1}) \end{bmatrix} + \begin{bmatrix} 0 \\ \omega_{es}\psi_{ms1} \\ 0 \\ 3\omega_{es}\psi_{ms3} \\ \hdashline 0 \\ \omega_{er}\psi_{mr} \end{bmatrix} \tag{4}$$

where u_x, i_x, and L_x ($x = ds1, qs1, ds3, qs3, dr, qr$) are the voltage, current, and inductance components under the dual rotating *d*–*q* frame, respectively. M_{sr} is the mutual inductance between the stator winding and the rotor winding. Note that the nondiagonal elements of the inductance matrix of the stator are all zero because the MTCM studied in this article embodies the hidden-pole characteristic, i.e., the *d*-axis inductance and the *q*-axis inductance of the five-phase stator are equal derived from finite-element analysis (FEA) analysis. ψ_{mr}, ψ_{ms1}, and ψ_{ms3}, are the PM flux linkage of the rotor windings, fundamental and third harmonic components of the stator windings. R_s and R_r are the stator and rotor winding resistance.

The electromagnetic torque of the MTCM can be derived as: (5), shown at the bottom of next page.

From the structure of the torque expression, the MTCM contains three parts of components, and therefore has higher torque density than that of the conventional PMSM in the same volume. The stator and rotor torque components are of the same nature as those of typical PMSMs. The mutual torque component is generated by the interaction between the stator and rotor currents and is therefore proportional to the mutual inductance. The torque expression can be further simplified. First, the salient polarity of the MTCM is relatively weak, i.e., the *dq*-axis inductance is basically equal. Second, the magnitude of the mutual inductance (10^{-3}) is relatively smaller than that of the flux (10^{-1}). Third, the back electromotive force (BMF) of the five-phase winding is not deliberately designed to be a trapezoidal wave, that is to say, the torque generated by i_{qs3} is relatively small. Based on the above three factors, the average torque expression can be simplified as

$$\begin{aligned} T_e &= \begin{bmatrix} \frac{5}{2}p_{ns}i_{qs1} & \frac{3}{2}p_{nr}i_{qr} \end{bmatrix} \begin{bmatrix} \psi_{ms1} \\ \psi_{mr} \end{bmatrix} \\ &= \underbrace{\frac{5}{2}p_{ns}i_{qs1}\psi_{ms1}}_{\mathrm{StatorTorqueComponentTes}} + \underbrace{\frac{3}{2}p_{nr}i_{qr}\psi_{mr}}_{\mathrm{RotorTorqueComponentTer}} \\ &= \frac{5}{2}p_{ns}i_{qs1}(\psi_{ss} + \psi_{sr}) + \frac{3}{2}p_{nr}i_{qr}(\psi_{rs} + \psi_{rr}) \\ &= \underbrace{\frac{5}{2}p_{ns}i_{qs1}\psi_{ss}}_{\mathrm{TorqueComponentA}} + \underbrace{\frac{5}{2}p_{ns}i_{qs1}\psi_{sr}}_{\mathrm{TorqueComponentB}} + \underbrace{\frac{3}{2}p_{nr}i_{qr}\psi_{rs}}_{\mathrm{TorqueComponentC}} \\ &\quad + \underbrace{\frac{3}{2}p_{nr}i_{qr}\psi_{rr}}_{\mathrm{TorqueComponentD}} . \end{aligned} \tag{6}$$

where $\psi_{ms1} = \psi_{ss} + \psi_{sr}$, $\psi_{mr} = \psi_{rs} + \psi_{rr}$, ψ_{ss} is the stator PM flux induced in the stator winding, ψ_{sr} is the rotor PM flux induced in the stator winding, ψ_{rs} is the stator PM flux induced in the rotor winding, and ψ_{rr} is the rotor PM flux induced in the rotor winding, respectively.

It can be seen that the generation of torque conforms to the principle of matrix multiplication. This is also the origin of the 'Matrix' in the name MTCM. The torque components included in the modified torque equation are consistent with the torque components in Fig. 1, which are torque components A, B, C, and D.

The mathematical model of MTCM contains mutual inductance M_{sr}, which is similar to dual three-phase machines [24]. It should be pointed out that there is no essential difference between the mathematical model of the flux modulation machine and the conventional PMSM [25]. The mutual torque generated

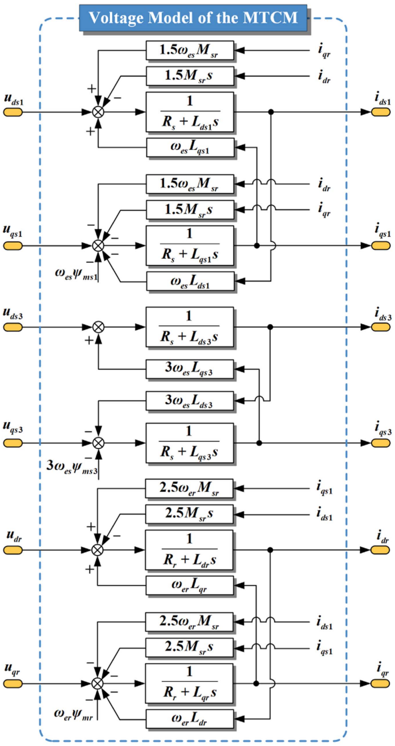

Fig. 3. Coupling structure of the MTCM voltage model.

by M_{sr} is very small and can be ignored. But the mutual inductance itself causes coupling in the machine current loop, which degrades the dynamic and steady state performance. Therefore, decoupling control is required.

III. ANALYSIS OF THE COUPLING AND HARMONIC DISTURBANCES OF THE MTCM

A. *Analysis of Coupling Terms*

In order to analyze the coupling condition of the MTCM more clearly, the Laplace operator s is introduced to perform the Laplace transform of (4). The voltage equation of the MTCM in the complex frequency domain can be expressed as (7).

Fig. 3 illustrates the different coupling terms of the MTCM voltage model according to (7). It is clearly that there are varying degrees of coupling between the various axes of the stator and rotor. Assuming that the machine is running in steady state and only the fundamental component of the current is considered, the current value is a constant. The coupling terms caused by the mutual inductance appear in the form of dc disturbances

$$\begin{cases} u_{ds1} = R_s i_{ds1} + sL_{ds1} i_{ds1} \\ \qquad + \underbrace{1.5sM_{sr}i_{dr} - \omega_{es}(L_{qs1}i_{qs1} + 1.5M_{sr}i_{qr})}_{\text{couplingterm}} \\ u_{qs1} = R_s i_{qs1} + sL_{qs1} i_{qs1} \\ \qquad \underbrace{+1.5sM_{sr}i_{qr} + \omega_{es}(L_{ds1}i_{ds1} + 1.5M_{sr}i_{dr} + \psi_{ms1})}_{\text{couplingterm}} \\ u_{ds3} = R_s i_{ds3} + sL_{ds3} i_{ds3} \\ \qquad \underbrace{-\,3\omega_{es}L_{qs3}i_{qs3}}_{\text{couplingterm}} \\ u_{qs3} = R_s i_{qs3} + sL_{qs3} i_{qs3} \\ \qquad + \underbrace{3\omega_{es}(L_{ds3}i_{ds3} + \psi_{ms3})}_{\text{couplingterm}} \\ u_{dr} = R_r i_{dr} + sL_{dr} i_{dr} \\ \qquad + \underbrace{2.5sM_{sr}i_{ds1} - \omega_{er}(L_{qr}i_{qr} + 2.5M_{sr}i_{qs1})}_{\text{couplingterm}} \\ u_{qr} = R_r i_{qr} + sL_{qr} i_{qr} \\ \qquad \underbrace{+2.5sM_{sr}i_{qs1} + \omega_{er}(L_{dr}i_{dr} + 2.5M_{sr}i_{ds1} + \psi_{mr})}_{\text{couplingterm}} \end{cases} . \tag{7}$$

B. *Analysis of Current Harmonics*

In the analysis of the previous section, only the fundamental component of the rotor/stator current and the third harmonic current of the stator current were considered. However, the phase current of the MTCM contains abundant other harmonic components due to the influence of nonideal factors, including

$$\begin{aligned} T_e = {} & \frac{5}{2}p_{ns}\Big[(L_{ds1} - L_{qs1})i_{ds1}i_{qs1} + \frac{3M_{sr}}{2}(i_{qs1}i_{dr} - i_{ds1}i_{qr}) + i_{qs1}\psi_{ms1} + 3(L_{ds3} - L_{qs3})i_{ds3}i_{qs3} \\ & + 3i_{qs3}\psi_{ms3}\Big] + \frac{3}{2}p_{nr}\Big[(L_{dr} - L_{qr})i_{dr}i_{qr} + \frac{5M_{sr}}{2}(i_{ds1}i_{qr} - i_{dr}i_{qs1}) + i_{qr}\psi_{mr}\Big] \\ = {} & \underbrace{\frac{5}{2}p_{ns}[(L_{ds1} - L_{qs1})i_{ds1}i_{qs1} + 3(L_{ds3} - L_{qs3})i_{ds3}i_{qs3} + i_{qs1}\psi_{ms1} + 3i_{qs3}\psi_{ms3}]}_{\text{Stator torque component}} \\ & + \underbrace{\frac{3}{2}p_{nr}[(L_{dr} - L_{qr})i_{dr}i_{qr} + i_{qr}\psi_{mr}]}_{\text{Rotortorquecomponent}} \\ & + \underbrace{\frac{15M_{sr}}{4}[p_{ns}(i_{qs1}i_{dr} - i_{ds1}i_{qr}) + p_{nr}(i_{ds1}i_{qr} - i_{dr}i_{qs1})]}_{\text{Mutual torque component}} . \end{aligned} \tag{5}$$

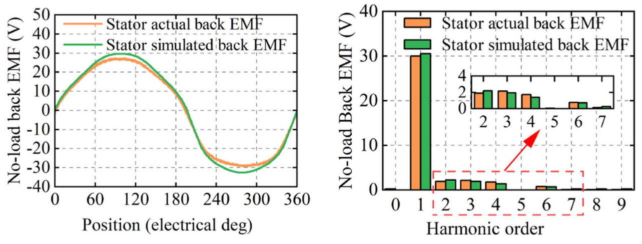

(a) (b)

Fig. 4. Comparison of simulation and experimental results of stator back EMF waveforms and FFT. (a) Back EMF waveforms. (b) FFT of back EMF.

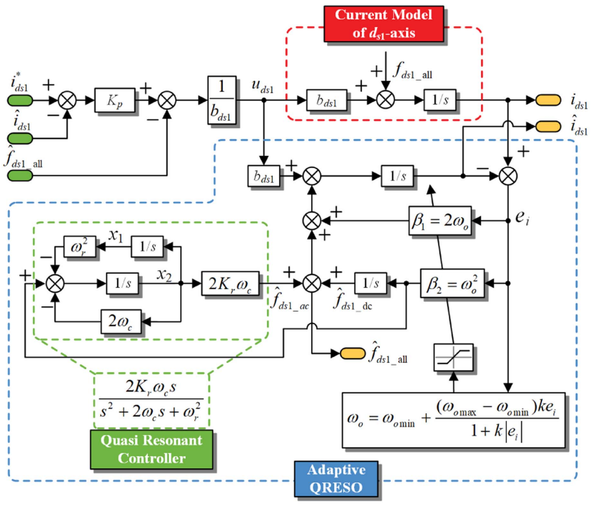

Fig. 5. Block diagram of the d_{s1}-axis adaptive QRESO.

the flux harmonics, inverter nonlinearity, winding distribution, and so on. The harmonics in the phase currents are reflected on the d_r-q_r and d_{s1}-q_{s1}-d_{s3}-q_{s3} frame and appear as ac disturbances, making the coupling of the MTCM more complicated. For the MTCM studied in this article, only the current harmonics caused by some of the factors are considered, as described later.

For the three-phase rotor, the fifth and seventh harmonics caused by inverter nonlinearity are mainly considered and suppressed in this article. According to the transformation calculation, the fifth and seventh harmonics in the three-phase current are mapped to the sixth harmonic on the d_r-q_r axis [26]. The rotor currents in the d_r-$q_r$axis considering harmonics can be derived as

$$\begin{cases} i_{dr} = I_{r1}\cos\theta_{r1} + I_{r5}\cos(6\omega_{er}t + \theta_{r5}) \\ \qquad\quad + I_{r7}\cos(6\omega_{er}t + \theta_{r7}) \\ i_{qr} = I_{r1}\sin\theta_{r1} - I_{r5}\sin(6\omega_{er}t + \theta_{r5}) \\ \qquad\quad + I_{r7}\sin(6\omega_{er}t + \theta_{r7}) \end{cases} \tag{8}$$

where I_{rg} and θ_{rg} $(g = 1, 5, 7)$ are the amplitude and phase angle of the nth current harmonic.

Due to the factors of slot-pole combination and winding design, the five-phase stator mainly contains even-order harmonics. The deeper reason is that the even-numbered winding factor is not zero. The detailed calculation process has already been derived in literature [7]. Fig. 4 shows the comparison of simulation and experimental results of the stator no-load back electromotive force (EMF) waveforms and fast Fourier transform (FFT) analysis. The simulation results are obtained by FEA. The speed of the simulation and experiment is set to rated 500 r/min.

The back EMF of the stator mainly contains second, third, fourth, and sixth harmonics. According to the voltage equation, the stator phase currents will also contain the harmonics of these orders. For five-phase machines, the third harmonic current can increase the torque. However, even-order harmonic currents do not contribute to torque. Therefore, the second, second, and sixth harmonic are mainly considered and suppressed in this article. The stator currents in the d_{s1}-q_{s1}-d_{s3}-q_{s3} axis considering harmonics can be derived as

$$\begin{cases} i_{ds1} = I_{s1}\cos\theta_{s1} + I_{s4}\cos(5\omega_{es}t + \theta_{s4}) \\ \qquad\quad + I_{s6}\cos(5\omega_{es}t + \theta_{s6}) \\ i_{qs1} = I_{s1}\sin\theta_{s1} - I_{s4}\sin(5\omega_{es}t + \theta_{s4}) \\ \qquad\quad + I_{s6}\sin(5\omega_{es}t + \theta_{s6}) \end{cases}$$
$$\begin{cases} i_{ds3} = I_{s3}\cos\theta_{s3} + I_{s2}\cos(5\omega_{es}t + \theta_{s2}) \\ i_{qs3} = I_{s3}\sin\theta_{s3} - I_{s2}\sin(5\omega_{es}t + \theta_{s2}) \end{cases} \tag{9}$$

where I_{sh} and θ_{sh} $(h = 2, 4, 6)$ are the amplitude and phase angle of the nth current harmonic. It should be noted that the second harmonic has no component on the d_{s1}-q_{s1} axis, but only on the d_{s3}-q_{s3} axis.

C. Current Loop Coupling Model Considering Both DC and AC Disturbances

Based on the aforementioned analysis, the current loop coupling model of MTCM considering dc and ac disturbances is developed. The voltage equation in time-domain can be rewritten as follows:

$$\begin{cases} p\boldsymbol{i}_{dqs1} = \boldsymbol{b}_{dqs1}\boldsymbol{u}_{dqs1} + \boldsymbol{f}_{dqs1\_dc} + \boldsymbol{f}_{dqs1\_ac} \\ p\boldsymbol{i}_{dqs3} = \boldsymbol{b}_{dqs3}\boldsymbol{u}_{dqs3} + \boldsymbol{f}_{dqs3\_dc} + \boldsymbol{f}_{dqs3\_ac} \\ p\boldsymbol{i}_{dqr} = \boldsymbol{b}_{dr}\boldsymbol{u}_{dr} + \boldsymbol{f}_{dr\_dc} + \boldsymbol{f}_{dr\_ac} \end{cases} \tag{10}$$

where p is the differential operator. i_x $(x = dqs1, dqs3, dqr)$ are the current vectors, $\boldsymbol{b}_x = \boldsymbol{1/L_x}$ are the coefficient vectors of system input. $\boldsymbol{f}_{x\_dc}$ are the aperiodic dc disturbance vectors caused by parameter mismatches and unmodeled disturbances. $\boldsymbol{f}_{x\_ac}$ are the periodic ac disturbance vectors embodied in current harmonics. The total disturbance $\boldsymbol{f}_{x\_all} = \boldsymbol{f}_{x\_dc} + \boldsymbol{f}_{x\_ac}$.

Considering both the mutual inductance and parameter mismatches, the expressions of $\boldsymbol{f_{x\_\mathrm{dc}}}$ are as follows:

$$
\begin{cases}
f_{ds1\_dc} = \Big[-(R_s + \Delta R_s) i_{ds1} - \Delta L_{ds1} p i_{ds1} \\
\quad -1.5(M_{sr} + \Delta M_{sr}) p i_{dr} \\
\quad + \omega_{es}\Big((L_{qs1} + \Delta L_{qs1}) i_{qs1} \\
\quad +1.5(M_{sr} + \Delta M_{sr}) i_{qr} \Big) \Big] / L_{ds1} + D_{ds1} \\
f_{qs1\_dc} = \Big[-(R_s + \Delta R_s) i_{qs1} - \Delta L_{qs1} p i_{qs1} \\
\quad -1.5(M_{sr} + \Delta M_{sr}) p i_{qr} \\
\quad - \omega_{es}\Big((L_{ds1} + \Delta L_{ds1}) i_{ds1} \\
\quad +1.5(M_{sr} + \Delta M_{sr}) i_{qr} + \psi_{ms1} \Big) \Big] / L_{qs1} + D_{qs1} \\
f_{ds3\_dc} = \Big[-(R_s + \Delta R_s) i_{ds3} - \Delta L_{ds3} p i_{ds3} \\
\quad +3\omega_{es}(L_{qs3} + \Delta L_{qs3}) i_{qs3} \Big] / L_{ds3} + D_{ds3} \\
f_{qs3\_dc} = \Big[-(R_s + \Delta R_s) i_{qs3} - \Delta L_{qs3} p i_{qs3} \\
\quad -3\omega_{es}((L_{ds3} + \Delta L_{ds3}) i_{ds3} + \psi_{ms3}) \Big] / L_{qs3} \\
f_{dr\_dc} = \Big[-(R_r + \Delta R_r) i_{dr} - \Delta L_{dr} p i_{dr} \\
\quad -2.5(M_{sr} + \Delta M_{sr}) p i_{ds1} \\
\quad + \omega_{er}\Big[(L_{qr} + \Delta L_{qr}) i_{qr} \\
\quad +2.5(M_{sr} + \Delta M_{sr}) i_{qs1} \Big] \Big] / L_{dr} + D_{dr} \\
f_{qr\_dc} = \Big[-(R_r + \Delta R_r) i_{qr} - \Delta L_{qr} p i_{qr} \\
\quad -2.5(M_{sr} + \Delta M_{sr}) p i_{qs1} \\
\quad - \omega_{er}\Big[(L_{dr} + \Delta L_{dr}) i_{dr} \\
\quad +2.5(M_{sr} + \Delta M_{sr}) i_{ds1} + \psi_{mr} \Big] \Big] / L_{qr} + D_{qr}
\end{cases}
\tag{11}
$$

where ΔR_s, ΔR_r, ΔM_{sr}, and ΔL_x characterize the parameter uncertainties. D_x characterizes the unmodelled disturbances.

The AC disturbance $\boldsymbol{f_{x\_\mathrm{ac}}}$ appears in the form of current harmonics. Using similar analyses as in [19], $\boldsymbol{f_{x\_\mathrm{ac}}}$ can be expressed as

$$
\boldsymbol{f_{x\_ac}} = \boldsymbol{g_x}(\boldsymbol{u_{x\_ac}}, \boldsymbol{\psi_{x\_ac}}, \boldsymbol{w_{x\_ac}}, \boldsymbol{p_{x\_ac}}) \tag{12}
$$

where $\boldsymbol{u_{x\_\mathrm{ac}}}$ is the ac disturbance vector caused by inverter nonlinearity, $\boldsymbol{\psi_{x\_\mathrm{ac}}}$ is the ac disturbance vector caused by flux harmonics, $\boldsymbol{w_{x\_\mathrm{ac}}}$ is the ac disturbance vector caused by winding factors, $\boldsymbol{p_{x\_\mathrm{ac}}}$ is the unmodelled ac disturbance vector.

It should be noted that the dc and ac unmodeled disturbance terms in the MTCM current loop coupling disturbance model include nonlinear factors, such as machine eddy current loss, temperature influence and skin effect. The decoupling method proposed in the following sections also takes the above nonlinear factors into consideration.

IV. IMPLEMENTATION OF THE PROPOSED METHODS FOR CURRENT LOOP CONTROL

Since the conventional LESO acts more like a lowpass filter for the disturbance observation, it cannot suppress the ac disturbance. In this section, an adaptive QRESO is proposed to suppress both the dc and ac disturbances simultaneously. The QRESO has two terms to estimate the disturbances. One is an integral term, and the other is an adaptive quasi-resonant controller. The integral term can estimate the dc disturbance, while the quasi-resonant controller can estimate the ac disturbance. Thus, the total disturbance can be estimated accurately and be feedforward compensated in the current loop.

A. *Design of the Proposed Adaptive QRESO*

Here, the QRESO is first designed as the d_{s1}-axis current controller. The rest of the current controllers are designed using the same method. Selecting i_{ds1} as the state variable, expanding the total unknown disturbance f_{ds1_all} into a new state variable, the state equation can be expressed as

$$
\begin{bmatrix} p i_{ds1} \\ p f_{ds1} \end{bmatrix} = \begin{bmatrix} 0 & 1 \\ 0 & 0 \end{bmatrix} \begin{bmatrix} i_{ds1} \\ f_{ds1\_all} \end{bmatrix} + \begin{bmatrix} b_{ds1} \\ 0 \end{bmatrix} u_{ds1} + \begin{bmatrix} 0 \\ 1 \end{bmatrix} h_{ds1} \tag{13}
$$

where $p f_{ds1\_\mathrm{all}} = h_{ds1}$.

The proposed QRESO is constructed as

$$
\begin{cases}
e_{ds1} = \hat{i}_{ds1} - i_{ds1} \\
p\hat{i}_{ds1} = \hat{f}_{ds1\_\mathrm{all}} - \beta_1 e_{ds1} + b_{ds1} u_{ds1} \\
\hat{f}_{ds1\_\mathrm{all}} = \hat{f}_{ds1\_dc} + \hat{f}_{ds1\_\mathrm{ac}} \\
p\hat{f}_{ds1\_dc} = -\beta_2 e_{ds1} \\
p x_1 = x_2 \\
p x_2 = -\beta_2 e_{ds1} - 2\omega_c x_2 - \omega_r^2 x_1 \\
\hat{f}_{ds1\_\mathrm{ac}} = 2K_r \omega_c x_2
\end{cases}
\tag{14}
$$

where ^ denotes the estimation value, e_{ds1} is the estimated current error, β_1, β_2 represent the observer gain, K_r is the gain of resonant controller, ω_r is the resonant frequency, and ω_c, x_1, and x_2 are the intermediate variables.

According the bandwidth-parameterization method of the conventional LESO [14], the observer gains can be derived as

$$
\beta_1 = 2\omega_o, \beta_2 = \omega_o^2 (\omega_o > 0) \tag{15}
$$

where ω_o is defined as the bandwidth of the observer.

The LESO need high gains to achieve fast converge and accurate observations. However, high gains may lead to poor noise suppression performance. Thus, the adaptive bandwidth is proposed, which can be designed as

$$
\omega_o = \omega_{o\,\min} + \frac{(\omega_{o\,\max} - \omega_{o\,\min}) k e_i}{1 + k\,|e_i|} \tag{16}
$$

where $\omega_{o\mathrm{min}}$, $\omega_{o\mathrm{max}}$, and k are the minimum value of ω_o, the maximum value of ω_o, and the positive constant, respectively.

Fig. 5 shows the block diagram of the current loop disturbance estimation scheme of the adaptive QRESO.

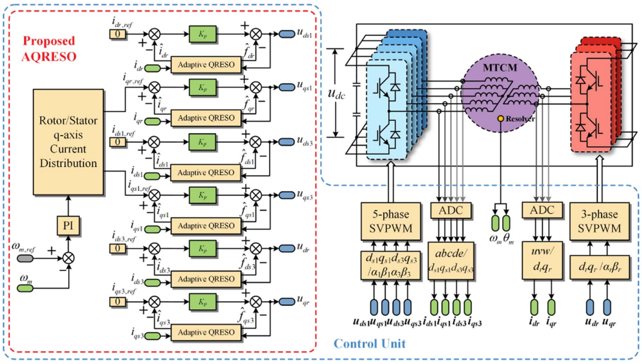

Fig. 6. Block diagram of the FOC-based MTCM drives with the proposed AQRESO.

Fig. 6 illustrates the block diagram of the FOC-based MTCM drives with the AQRESO. The speed loop is adjusted by the PI controller, which outputs the stator and rotor total q-axis current. The current distribution module is used to distribute the ratio of the stator $qs1$-axis and rotor qr-axis currents. In this article, i_{ds1}, i_{ds3}, i_{qs3}, and i_{dr} are all set to 0, and let $i_{qs1,\mathrm{ref}} = i_{qr,\mathrm{ref}}$, considering that the reluctance torque and third harmonic torque can be ignored compared with the synchronous torque according to torque (6).

The QRESO controller design of each axis is the same as Fig. 5. According to the analysis in Chapter III, the resonant frequencies of the d_r-q_r axes are six times that of ω_{er}, and the resonant frequencies of the d_{s1}-q_{s1}-d_{s3}-q_{s3} axes are five times that of ω_{es}.

B. Harmonic Suppression Capability Analysis of the Proposed Adaptive QRESO in Current-Loop System

To analyze the harmonic rejection capability of the entire current-loop system, the transfer function from the actual total disturbance to the output d_{s1}-axis current is derived in this part. Based on (14), the QRESO of d_{s1}-axis in frequency-domain can be derived as

$$\begin{cases} E_{ds1}(s) = \hat{I}_{ds1}(s) - I_{ds1}(s) \\ \hat{I}_{ds1}(s) = \frac{1}{s}(\hat{F}_{ds1\_all}(s) - \beta_1 E_{ds1}(s) + b_{ds1}U_{ds1}(s)) \\ \hat{F}_{ds1\_all}(s) = -\left(G_{QR}(s) + \frac{1}{s}\right)\beta_2 E_{ds1}(s) \\ G_{QR}(s) = \frac{2K_r\omega_c s}{s^2+2\omega_c s+\omega_r^2} \end{cases}. \tag{17}$$

According to (17), the transfer function from the actual total disturbance to the total estimated disturbance can be deduced as

$$G_F(s) = \frac{\hat{F}_{ds1\_all}}{F_{ds1\_all}} = \frac{\beta_2 + \beta_2 G_{QR}(s)s}{s^2 + \beta_1 s + \beta_2 + \beta_2 G_{QR}(s)s} = \frac{\delta(s)}{\lambda(s)}. \tag{18}$$

Substituting (15) into (18), then the expression of $\delta(s)$ and $\lambda(s)$ can be derived as

$$\begin{aligned} \delta(s) &= (2K_r\omega_c\omega_o^2 + \omega_o^2)s^2 + 2\omega_o^2\omega_c s + \omega_o^2\omega_r^2 \\ \lambda(s) &= s^4 + 2(\omega_c + \omega_o)s^3 + (4\omega_o\omega_c + 2\omega_o^2 K_r\omega_c + \omega_o^2 \\ &\quad + \omega_r^2)s^2 + 2\omega_o(\omega_r^2 + \omega_o\omega_c)s + \omega_o^2\omega_r^2. \end{aligned} \tag{19}$$

Based on Fig. 5, the control law of the current-loop in frequency-domain can be derived as

$$U_{ds1}(s) = \frac{K_p(i_{ds1}^* - \hat{I}_{ds1}(s)) - \hat{F}_{ds1\_all}(s)}{b_{ds1}}. \tag{20}$$

Assuming the reference d_{s1}-axis current $i_{ds1}{}^*$ to be zero. Joint (20) and (17), the following expression can be obtained as

$$b_{ds1}U_{ds1}(s) = -\hat{F}_{ds1\_all}(s) - \frac{K_p\beta_1 s\hat{F}_{ds1\_all}(s)}{(K_p+s)(sG_{QR}(s)+1)\beta_2}. \tag{21}$$

The current model of d_{s1}-axis in frequency-domain can be expressed as

$$sI_{ds1}(s) = b_{ds1}U_{ds1}(s) + F_{ds1\_all}(s). \tag{22}$$

Substituting (21) into (22) yields

$$\begin{aligned} I_{ds1}(s) &= \frac{F_{ds1\_all}(s)}{s} - \frac{K_p\beta_1\hat{F}_{ds1\_all}(s)}{(s+K_p)[sG_{QR}(s)+1]\beta_2} \\ &\quad - \frac{\hat{F}_{ds1\_all}}{s+K_p} - \frac{K_p\hat{F}_{ds1\_all}(s)}{s(s+K_p)}. \end{aligned} \tag{23}$$

Substituting (18) into (23), the transfer function from the actual total disturbance to the output d_{s1}-axis current can be derived as

$$\begin{aligned} G_I(s) &= \frac{I_{ds1}(s)}{F_{ds1\_all}(s)} \\ &= \frac{s^2 + (\beta_1 + K_p)s}{(s^2 + \beta_1 s + \beta_2 + \beta_2 G_{QR}(s)s)(K_p + s)} \\ &= \frac{s^2 + (2\omega_o + K_p)s}{(s^2 + 2\omega_o s + \omega_o^2 + \omega_o^2 G_{QR}(s)s)(K_p + s)}. \end{aligned} \tag{24}$$

The bode plots of $G_I(s)$ for different ω_r, ω_o, and K_p are shown in Fig. 7.

The bode plots show the superiority of the AQRESO in suppressing harmonic disturbances. The magnitude at the harmonic frequency is extremely small, which means that if the current loop has harmonic disturbance input, the output current will not contain the harmonic of this frequency.

V. STABILITY ANALYSIS OF THE PROPOSED METHOD

A. Stability Analysis of the Adaptive QRESO

In order to implement the adaptive QRESO digitally, the observer should be transformed into discrete time form. Based on (17) and using the forward Euler method, the discrete time form of the QRESO can be deduced by

$$\begin{bmatrix} \hat{I}_{ds1}(k+1) \\ \hat{F}_{ds1\_all}(k+1) \end{bmatrix} = \boldsymbol{A_{QR}} \begin{bmatrix} \hat{I}_{ds1}(k) \\ \hat{F}_{ds1\_all}(k) \end{bmatrix} + \begin{bmatrix} T_s\beta_1 I_{ds1}(k) + T_s b_{ds1}U_1(k) \\ \beta_2[(z-1)G_{QR}(z) + T_s]I_{ds1}(k) \end{bmatrix} \tag{25}$$

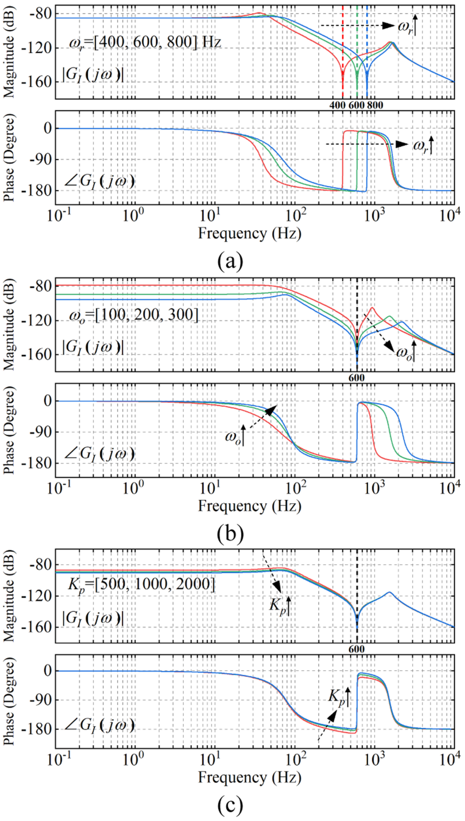

(a)

(b)

(c)

Fig. 7. Bode plot of G_I(s) under different parameters. (a) $\omega_r = [400, 600, 800]$ Hz. (b) $\omega_o = [100, 200, 300]$. (c) $K_p = [500, 1000, 2000]$.

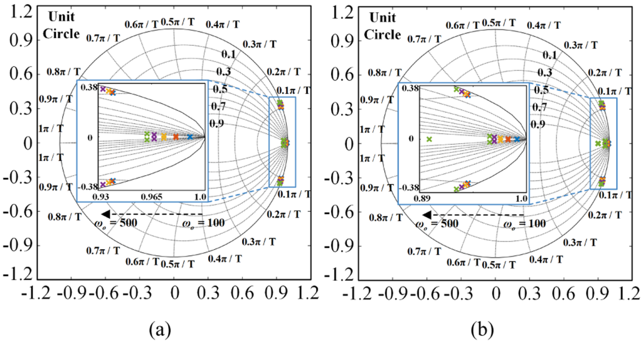

(a)

(b)

Fig. 8. (a) Characteristic roots distribution of $\Delta_0(z) = 0$ with ω_o varies from 100 to 500. (b) Characteristic roots distribution of Δ_1(z) = 0 with ω_o varies from 100 to 500.

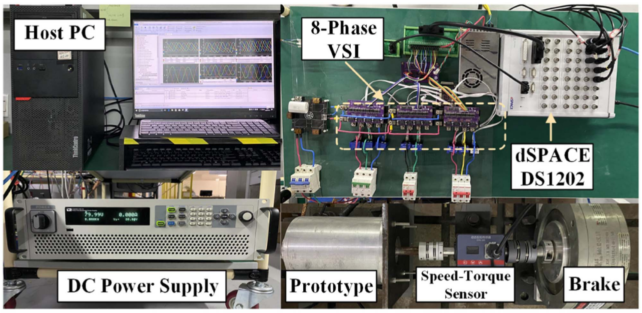

Fig. 9. Experimental platform.

where

$$\boldsymbol{A_{QR}} = \begin{bmatrix} 1 - T_s\beta_1 & T_s \\ -\beta_2[(z-1)G_{QR}(z) + T_s] & 1 \end{bmatrix}$$

$$G_{QR}(z) = \frac{2K_r\omega_c T_s(z-1)}{(z-1)^2 + 2\omega_c T_s(z-1) + T_s^2\omega_r^2} \tag{26}$$

where T_s is the system sampling time.

To determine whether the discrete QRESO is stable, it is necessary to determine whether all the eigenvalues of matrix $\boldsymbol{A_{QR}}$ are inside the unit circle of z plane. The characteristic equation of $\boldsymbol{A_{QR}}$ is derived as

$$\det(z\boldsymbol{I} - \boldsymbol{A_{QR}}) = 0. \tag{27}$$

Substituting (26) into (27), the characteristic equation is equivalent to

$$\Delta_0(z) = a_4 z^4 + a_3 z^3 + a_2 z^2 + a_1 z + a_0 = 0 \tag{28}$$

where

$$\begin{cases} a_0 = -2\omega_c\beta_2 T_s^3 + 2\omega_c\beta_1 T_s^2 + 2K_r\omega_c\beta_2 T_s^2 + \beta_2 T_s^2 \\ \qquad - 2\omega_c T_s - \beta_1 T_s + 1 \\ a_1 = \beta_2\omega_r^2 T_s^4 + 2\omega_c\beta_2 T_s^3 - \beta_1\omega_r^2 T_s^3 - 4\omega_c\beta_1 T_s^2 \\ \qquad -4K_r\omega_c\beta_2 T_s^2 + \omega_r^2 T_s^2 \\ \qquad -2\beta_2 T_s^2 + 6\omega_c T_s + 3\beta_1 T_s - 4 \\ a_2 = \beta_1\omega_r^2 T_s^3 + 2\omega_c\beta_1 T_s^2 + 2K_r\omega_c\beta_2 T_s^2 + \beta_2 T_s^2 \\ \qquad -2\omega_r^2 T_s^2 - 6\omega_c T_s - 3\beta_1 T_s + 6 \\ a_3 = \omega_r^2 T_s^2 + 2\omega_c T_s + \beta_1 T_s - 4 \\ a_4 = 1 \end{cases}. \tag{29}$$

Fig. 8(a) describes the characteristic roots distribution of Δ_0(z). All roots locate inside the unit circle with the change of ω_o. Therefore, the QRESO is stable.

B. Stability Analysis of the Current-Loop With the Proposed Adaptive QRESO

Based on (17) and (22), the discrete time form of the whole current closed-loop system can be expressed as

$$\begin{bmatrix} I_{ds1}(k+1) \\ \hat{I}_{ds1}(k+1) \\ \hat{F}_{ds1\_all}(k+1) \end{bmatrix} = \boldsymbol{A_{CL}} \begin{bmatrix} I_{ds1}(k) \\ \hat{I}_{ds1}(k) \\ \hat{F}_{ds1\_all}(k) \end{bmatrix} + \begin{bmatrix} T_s F_{ds1\_all}(k) + K_p i_{ds1}^* \\ T_s K_p i_{ds1}^* \\ 0 \end{bmatrix} \tag{30}$$

where

$$\boldsymbol{A_{CL}} = \begin{bmatrix} 1 & -T_s K_p & -T_s \\ T_s\beta_1 & 1-T_s\beta_1-T_s K_p & 0 \\ \beta_2[(z-1)G_{QR}(z)+T_s] & -\beta_2[(z-1)G_{QR}(z)+T_s] & 1 \end{bmatrix}. \tag{31}$$

The stability of the current closed-loop system is dependent on the eigenvalues of matrix $\boldsymbol{A_{CL}}$. The characteristic equation of $\boldsymbol{A_{CL}}$ is derived as

$$\det(z\boldsymbol{I} - \boldsymbol{A_{CL}}) = 0. \tag{32}$$

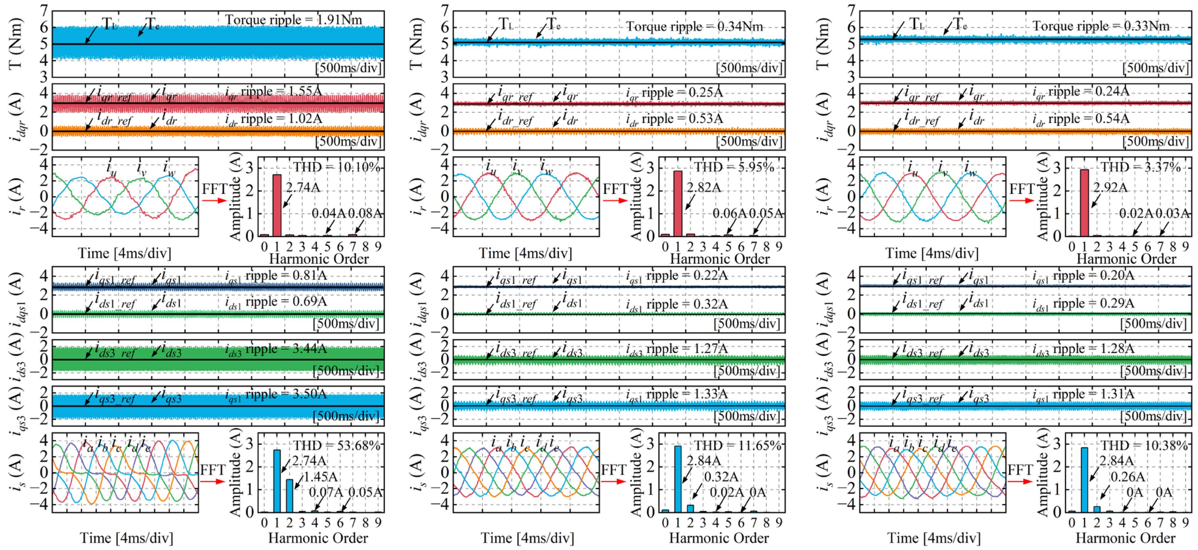

(a) (b) (c)

Fig. 10. Comparative experimental results of torque, current waveform and current FFT analysis of three methods at 500 r/min and 5 N·m load. (a) Traditional PI controller. (b) GIESO method. (c) Proposed AQRESO method.

Substituting (31) into (32), the characteristic equation is equivalent to

$$\Delta_1(z) = h_5 z^5 + h_4 z^4 + h_3 z^3 + h_2 z^2 + h_1 z + h_0 = 0 \quad (33)$$

where

$$\begin{cases} h_0 = T_s\beta_1 + T_sK_p + 2T_s\omega_c - T_s^2\beta_2 \\ \qquad -\omega_r^2T_s^2 + \beta_1\omega_r^2T_s^3 - \beta_2\omega_r^2T_s^4 \\ \qquad + K_p\omega_r^2T_s^3 - K_p\beta_1T_s^2 + K_p\beta_2T_s^3 \\ \qquad -2\beta_1\omega_cT_s^2 + 2\beta_2\omega_cT_s^3 \\ \qquad - 2K_p\omega_cT_s^2 + 2K_p\omega_c\beta_1T_s^3 \\ \qquad -2K_p\omega_c\beta_2T_s^4 - 2\beta_2K_r\omega_cT_s^2 \\ \qquad -K_p\beta_1\omega_r^2T_s^4 + K_p\beta_2\omega_r^2T_s^5 + 2K_pK_r\beta_2\omega_cT_s^3 - 1 \\ h_1 = 3\beta_2T_s^2 - 4T_sK_p - 8T_s\omega_c - 4T_s\beta_1 \\ \qquad +3\omega_r^2T_s^2 - 2\beta_1\omega_r^2T_s^3 \\ \qquad + \beta_2\omega_r^2T_s^4 - 2K_p\omega_r^2T_s^3 + 3K_p\beta_1T_s^2 \\ \qquad -2K_p\beta_2T_s^3 + 6\beta_1\omega_cT_s^2 \\ \qquad - 4\beta_2\omega_cT_s^3 + 6K_p\omega_cT_s^2 - 4K_p\omega_c\beta_1T_s^3 \\ \qquad +2K_p\omega_c\beta_2T_s^4 + 6\beta_2K_r\omega_cT_s^2 + K_p\beta_1\omega_r^2T_s^4 \\ \qquad -4K_pK_r\beta_2\omega_cT_s^3 + 5 \\ h_2 = 6T_s\beta_1 + 6T_sK_p + 12T_s\omega_c - 3T_s^2\beta_2 \\ \qquad -3\omega_r^2T_s^2 + \beta_1\omega_r^2T_s^3 + K_p\omega_r^2T_s^3 \\ \qquad - 3K_p\beta_1T_s^2 + K_p\beta_2T_s^3 - 6\beta_1\omega_cT_s^2 \\ \qquad +2\beta_2\omega_cT_s^3 - 6T_s^2K_p\omega_c \\ \qquad + 2K_p\omega_c\beta_1T_s^3 - 6\beta_2K_r\omega_cT_s^2 \\ \qquad +2K_pK_r\beta_2\omega_cT_s^3 - 10 \\ h_3 = T_s^2\beta_2 - 4T_sK_p - 8T_s\omega_c - 4T_s\beta_1 + \omega_r^2T_s^2 \\ \qquad +K_p\beta_1T_s^2 + 2\beta_1\omega_cT_s^2 \\ \qquad + 2K_p\omega_cT_s^2 + 2\beta_2K_r\omega_cT_s^2 + 10 \\ h_4 = \beta_1T_s + K_pT_s + 2\omega_cT_s - 5 \\ h_5 = 1 \end{cases} . \quad (34)$$

TABLE I
PARAMETERS OF THE PROTOTYPE

Parameters	Value	Parameters	Value
Rated power (kW)	0.3	Rated stator current (A)	2.5
DC-bus voltage (V)	80	R_s (Ω)	0.754
Rated speed (rpm)	500	R_r (Ω)	0.506
Rated torque (Nm)	5	L_{ds1}, L_{qs1} (mH)	6.315
Stator slot number	10	L_{ds3}, L_{qs3} (mH)	1.177
Rotor slot number	12	L_{dr}, L_{qr} (mH)	4.005
Rated rotor current (A)	2.5	M_{sr} (mH)	2.280

Fig. 8(b) describes the characteristic roots distribution of Δ_1(z). All roots locate inside the unit circle with the change of ω_o. Therefore, the whole current loop system is stable.

VI. EXPERIMENT RESULTS

To verify the feasibility and validity of the proposed scheme, the experiments are carried out on a stator 5-phase, 10-slot, rotor 3-phase, 12-slot MTCM prototype. The parameters of the MTCM prototype are given in Table I. The MTCM is driven by a self-developed eight-phase voltage source inverter, and the control scheme is implemented with a dSPACE DS1202 system. The three-phase rotor winding is powered by slip rings and brushes. The position signal is read by the resolver. The sampling frequency and the PWM frequency are both 10 kHz. The experiment setup is shown in Fig. 9. The parameters of the current loop control system are given in Table II.

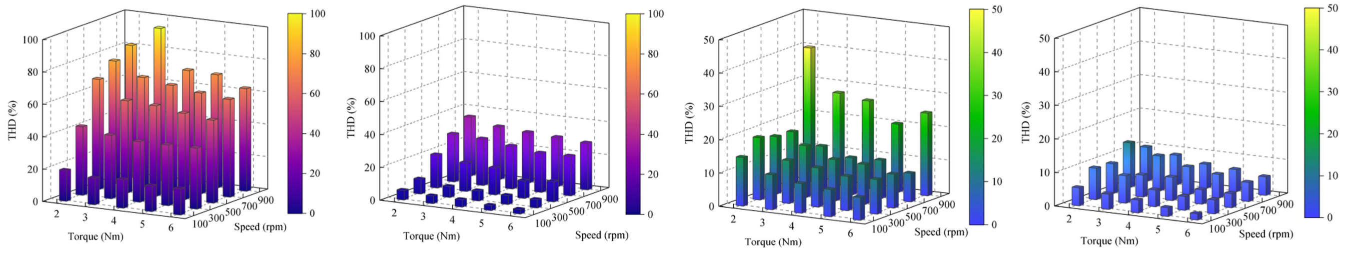

(a) (b) (c) (d)

Fig. 11. Comparative experimental results of the MTCM stator and rotor current THDs under different speed and load torque. (a) Stator THD results of traditional PI controller. (b) Stator THD results of AQRESO method. (c) Rotor THD results of traditional PI controller. (d) Rotor THD results of AQRESO method.

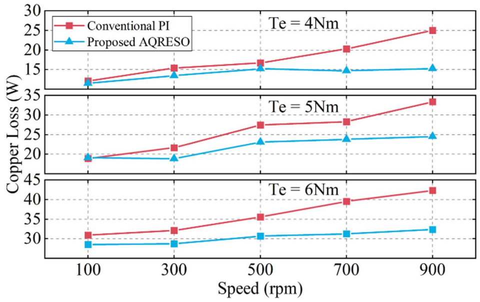

Fig. 12. Comparative experimental results of MTCM copper loss at different speeds when the load torque is 4, 5, and 6 N·m.

TABLE II
PARAMETERS OF THE CURRENT LOOP CONTROL SYSTEM

Parameters	Symbols	Value of Stator $ds1$-$qs1$ axis	Value of Stator $ds3$-$qs3$ axis	Value of Rotor dr-qr axis
Forward gain	K_p	5200	5200	2000
Minimum QRESO bandwidth	$\omega_{o\min}$	100	100	100
Maximum QRESO bandwidth	$\omega_{o\max}$	500	400	500
Adaptive gain	k	0.12	0.15	0.25
Resonant Frequency	ω_r	$5\omega_{es}$	$5\omega_{es}$	$6\omega_{er}$
Resonant bandwidth	ω_c	600	500	500
Resonant gain	K_r	0.01	0.01	0.01

A. Steady-State Performance Verification

To verify the decoupling and harmonics suppression capability of the proposed AQRESO method, the steady-state experimental results are obtained under the conditions of rated speed and rated load torque. In order to make the comparison of experimental results more comprehensive, the PI controller and the generalized integrator-based ESO (GIESO) method are selected for comparison with the proposed method in this article. The recent control schemes for MTCM (and some novel machines with similar structures) are mostly related to fault-tolerant control [10], [11]. However, the current loop regulators of these fault-tolerant control methods are still traditional PI controllers. Therefore, the use of PI controller as a comparative experiment for the method proposed in this article can better reflect the improvement of MTCM control characteristics. The compared GIESO method [27] reported in the recent literatures is similar to the QRESO studied in this article in structure and principle. By setting the resonant frequency of the GIESO, the periodic disturbance can be observed and compensated, thereby reducing harmonics [28].

TABLE III
COMPARISON OF CURRENT RIPPLE AND HARMONICS BASED ON THREE CONTROLLERS

Method		PI	GIESO	AQRESO
Torque Ripple (Nm)		1.91	0.34	0.33
Current Ripple (A)	i_{dr} ripple	1.02	0.53	0.54
	i_{qr} ripple	1.55	0.25	0.24
	i_{ds1} ripple	0.69	0.32	0.29
	i_{qs1} ripple	0.81	0.22	0.20
	i_{ds3} ripple	3.44	1.27	1.28
	i_{qs3} ripple	3.50	1.33	1.31
Rotor Harmonic Current Amplitude (A)	5th	0.04	0.06	0.05
	7th	0.08	0.05	0.03
Stator Harmonic Current Amplitude (A)	2nd	1.45	0.32	0.26
	4th	0.07	0.02	0
	6th	0.05	0	0

Fig. 10 shows the comparative experimental results of torque, d_r-q_r-d_{s1}-q_{s1}-d_{s3}-q_{s3} axes current waveforms, and FFT analysis of the stator/rotor phase current of the aforementioned three methods. From the FFT results of the PI controller in Fig. 10(a), it is obvious that there are fifth and seventh harmonics in the rotor phase current. As for the stator phase current, there are second, fourth, and sixth harmonics. These results are consistent with the theoretical analysis in Section III. Since the PI controller does not have the ability to suppress harmonics, the THD of the phase current is relatively high. In addition, the d–q axes current ripple leads to relatively large torque ripple, reaching 1.91 N·m.

The FFT analysis in Fig. 10(b) and (c) show that both the GIESO method and the AQRESO method can suppress current harmonics. The performance of the AQRESO is slightly better than GIESO. The harmonic suppression capability of the proposed AQRESO for the specified harmonics is consistent with that shown in the Bode plots (see Section IV, Fig. 7). The ripple of the d–q axes current has been effectively suppressed. The torque ripple is reduced to 0.34 and 0.33 N·m, respectively. To clearly illustrate the advantages of the proposed method, some data related to the torque ripple, current ripple and harmonics are given in Table III. The experimental results show

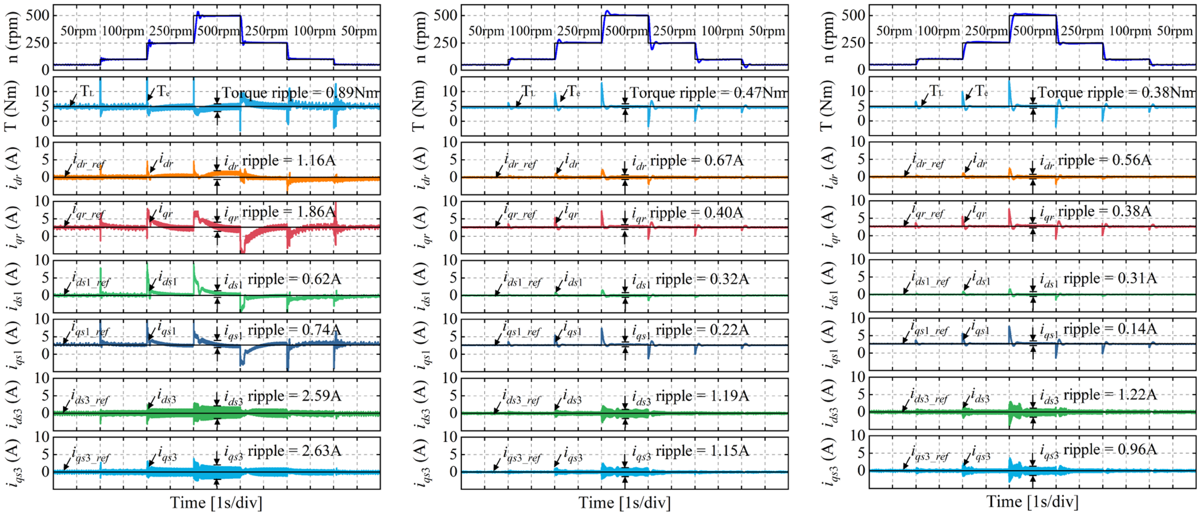

(a) (b) (c)

Fig. 13. Comparative experimental results of speed, torque, and d_r -q_r -d_{s1}-q_{s1}-d_{s3}-q_{s3} axes current waveforms under speed step from 50 to 500 r/min. (a) Traditional PI controller. (b) GIESO method. (c) Proposed AQRESO method.

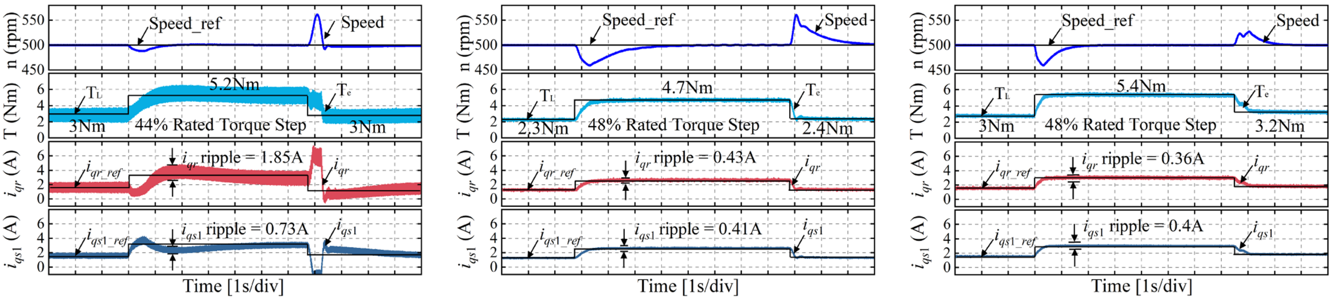

(a) (b) (c)

Fig. 14. Comparative experimental results of speed, torque, q-axes current waveforms under torque step of 44% or 48% rated load torque. (a) Traditional PI controller. (b) GIESO method. (c) Proposed AQRESO method.

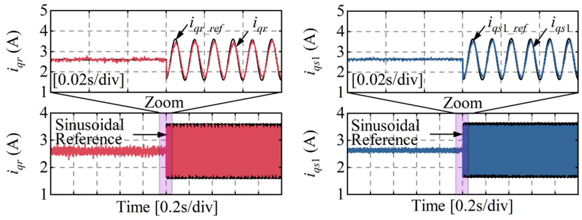

(a) (b)

Fig. 15. Experimental results of q-axes current in tracking sinusoidal reference. (a) Rotor side response. (b) Stator side response.

that the AQRESO effectively suppresses the dc and ac disturbances in steady state and achieves the purpose of current loop decoupling.

In order to further verify the effectiveness of the proposed method on harmonic suppression ability under different working conditions, Fig. 11 shows the comparative experimental results of the MTCM stator and rotor current THDs under different speed and load torque. The proposed AQRESO method can effectively reduce phase current harmonics regardless of low speed or high speed, heavy load or light load.

To further discuss the impact of current harmonics on the operating performance of MTCM, Fig. 12 illustrates the copper loss comparison experimental results of the traditional PI and the proposed method under different working conditions.

Since harmonic current has almost no contribution to torque, the proposed method can effectively reduce copper loss under the same working conditions. This effect becomes more obvious as the speed increases, because according to the previous experimental results, the current THD of MTCM increases as the speed increases.

B. Dynamic Response Performance Verification

In order to verify the dynamic response performance of MTCM with the proposed method, speed dynamic experiments and torque dynamic experiments are carried out in this part. Fig. 13 shows the comparative experimental results of speed, torque, and d_r-q_r-d_{s1}-q_{s1}-d_{s3}-q_{s3} axes current waveforms under the speed step from 50 to 500 r/min.

Firstly, the performance of MTCM under low speed and low step jump value conditions are analyzed, that is, the speed steps from 50 to 100 r/min. The speed overshoots of the traditional PI controller, the GIESO method and the proposed method are 13.14%, 12.21%, and 1.74% respectively. The settling time of the three methods is 0.072s, 0.218, and 0.170 s, respectively. The standard deviations of the three methods are 1.099, 0.927, and 0.900, respectively. As for the performance at high speed and high jump value, that is, the speed steps from 250 to 500 r/min. The speed overshoots of the three methods are 7.52%, 9.11%, and 3.62% respectively. The settling time of the three methods is 0.261, 0.325, and 0.253 s, respectively. The standard deviations of the three methods are 2.875, 2.957, and 3.018, respectively.

In summary, regardless of the low speed and low step jump value condition or the high speed and high step jump value condition, the overshoot of the proposed AQRESO is the lowest. As for the settling time, the proposed method is similar to the traditional PI controller under various conditions, but is faster than the GIESO method. The reason is that the ESO gain parameter of the proposed method has an adaptive algorithm, which improves robustness. The comparison of standard deviations shows that the three methods have similar ability to follow the reference speed, and the errors are all within an acceptable range.

Fig. 14 shows the comparative experimental results of speed, torque, q-axes current waveforms under torque step when the reference speed remains 500 r/min. The torque jump value is set to approximately half of the rated load torque. When the torque increases, the torque settling time of the three methods is 0.98, 0.61, and 0.52 s, respectively. The speed fluctuations of the three methods are 17, 38, and 38 r/min, respectively. When the torque decreases, the speed fluctuations of the three methods are 61, 60, and 24 r/min, respectively. Overall, the proposed method has the best torque dynamic regulation performance. The advantage of the GIESO and AQRESO methods over the traditional PI controller is more reflected in the smaller ripple of the electromagnetic torque.

Fig. 15 illustrates the tracking capability of the proposed AQRESO method for the sinusoidal reference current value. The reference rotor q_r -axis and stator q_{s1}-axis current are both set to 2.5+sin (200 π) A. As can be seen, the proposed AQRESO method has good tracking performance for sinusoidal reference current. The amplitude and phase of the sinusoidal feedback current are consistent with the given value. The good tracking performance of the q-axes current indirectly reflects the effectiveness of the current loop decoupling control.

VII. CONCLUSION

In this article, the current loop decoupling method based on AQRESO for a novel MTCM is studied. The harmonic suppression performance and stability of the proposed method are analyzed in detail. The proposed method can adapt well to the characteristics of the novel MTCM. The proposed AQRESO can observe and compensate for the dc coupling terms caused by the mutual inductance of the machine in the current loop, thereby improving the dynamic performance. It can also observe and compensate for the phase current harmonics caused by nonlinear factors and special winding structure, reduce current ripple, and thus improve the steady-state performance. According to experimental validation, the decoupling performance of the proposed method is superior to that of the traditional PI controller, and is slightly better than the existing GIESO method. Meanwhile, the proposed method has better dynamic response performance compared to the traditional PI controller and the GIESO method due to the adaptive algorithm of the observer gain.

REFERENCES

[1] C. Liu, K. T. Chau, C. H. T. Lee, and Z. Song, "A critical review of advanced electric machines and control strategies for electric vehicles," *Proc. IEEE*, vol. 109, no. 6, pp. 1004–1028, Jun. 2021, doi: 10.1109/JPROC.2020.3041417.

[2] Z. Jiao, Z. Li, Y. Shang, S. Wu, Z. Song, and Q. Pan, "Active load sensitive electro-hydrostatic actuator on more electric aircraft: Concept, design, and control," *IEEE Trans. Ind. Electron.*, vol. 69, no. 5, pp. 5030–5040, May 2022, doi: 10.1109/TIE.2021.3084179.

[3] P. Ojaghlu and A. Vahedi, "Specification and design of ring winding axial flux motor for RIM-driven thruster of ship electric propulsion," *IEEE Trans. Veh. Technol.*, vol. 68, no. 2, pp. 1318–1326, Feb. 2019, doi: 10.1109/TVT.2018.2888841.

[4] L. Wu, Y. Zheng, Y. Fang, and X. Huang, "Novel fault-tolerant doubly fed flux reversal machine with armature windings wound on both stator and rotor teeth," *IEEE Trans. Ind. Electron.*, vol. 68, no. 6, pp. 4780–4789, Jun. 2021, doi: 10.1109/TIE.2020.2989721.

[5] J. Huang, W. Fu, S. Niu, X. Zhao, and Y. Bi, "A novel dual-side PM machine with decoupled stator PM topology," *IEEE Trans. Ind. Electron.*, vol. 71, no. 12, pp. 15301–15312, Dec. 2024, doi: 10.1109/TIE.2024.3383009.

[6] P. Sun, S. Jia, D. Yang, Z. Liu, and D. Liang, "Analysis of a novel dual winding dual magnet machine with compound fault-tolerance capability," *IEEE Trans. Ind. Electron.*, vol. 71, no. 12, pp. 15424–15434, Dec. 2024, doi: 10.1109/TIE.2024.3390724.

[7] P. Sun, S. Jia, D. Yang, and D. Liang, "Comparative study of novel dual winding dual magnet flux modulated machines with different stator/rotor pole combinations," *IEEE Trans. Transp. Electrific.*, vol. 10, no. 4, pp. 9691–9700, Dec. 2024, doi: 10.1109/TTE.2024.3377454.

[8] N. Argibay, J. A. Bares, J. H. Keith, G. R. Bourne, and W. G. Sawyer, "Copper–beryllium metal fiber brushes in high current density sliding electrical contacts," *Wear*, vol. 268, no. 11–12, pp. 1230–1236, 2010.

[9] W. Zhai et al., "Recent progress on wear-resistant materials: Designs, properties, and applications," *Adv. Sci.*, vol. 8, no. 11, Jun. 2021, Art. no. 2003739, doi: 10.1002/advs.202003739.

[10] S. Jia, D. Yang, P. Sun, and D. Liang, "Open circuit fault-tolerant control of novel matrix-torque-component machines based on multiple operation modes," *IEEE Trans. Transp. Electrific.*, to be published, doi: 10.1109/TTE.2024.3487151.

[11] J. Yi, L. Wu, Y. Lu, Z. Qi, W. Zheng, and T. Zheng, "Fault-tolerant operation for single-phase open circuit of dual-armature flux-switching permanent magnet machine by connecting neutral points," *IEEE Trans. Transp. Electrific.*, vol. 11, no. 1, pp. 2952–2964, Feb. 2025., doi: 10.1109/TTE.2024.3431271.

[12] M. Elkayam, S. Kolesnik, and A. Kuperman, "Guidelines to classical frequency-domain disturbance observer redesign for enhanced rejection of periodic uncertainties and disturbances," *IEEE Trans. Power Electron.*, vol. 34, no. 4, pp. 3986–3995, Apr. 2019, doi: 10.1109/TPEL.2018.2865688.

[13] J. Yang, W. -H. Chen, S. Li, L. Guo, and Y. Yan, "Disturbance/uncertainty estimation and attenuation techniques in PMSM drives—A survey," *IEEE Trans. Ind. Electron.*, vol. 64, no. 4, pp. 3273–3285, Apr. 2017, doi: 10.1109/TIE.2016.2583412.

[14] Z. Gao, "Scaling and bandwidth-parameterization based controller tuning," in *Proc. Amer. Control Conf.*, Jun. 2003, pp. 4989–4996. doi: 10.1109/ACC.2003.1242516.

[15] P. Kumar, A. R. Beig, D. V. Bhaskar, K. A. Jaafari, U. R. Muduli, and R. K. Behera, "An enhanced linear active disturbance rejection controller for high performance PMBLDCM drive considering iron loss," *IEEE*

Trans. Power Electron., vol. 36, no. 12, pp. 14087–14097, Dec. 2021, doi: 10.1109/TPEL.2021.3088418.

[16] M. Tian, B. Wang, Y. Yu, Q. Dong, and D. Xu, “Discrete-time repetitive control-based ADRC for current loop disturbances suppression of PMSM drives,” *IEEE Trans. Ind. Informat.*, vol. 18, no. 5, pp. 3138–3149, May 2022, doi: 10.1109/TII.2021.3107635.

[17] L. Romeral, J. C. Urresty, J.-R. R. Ruiz, and A. G. Espinosa, “Modeling of surface-mounted permanent magnet synchronous motors with stator winding interturn faults,” *IEEE Trans. Ind. Electron.*, vol. 58, no. 5, pp. 1576–1585, May 2011, doi: 10.1109/TIE.2010.2062480.

[18] W. Xu, R. Dian, Y. Liu, D. Hu, and J. Zhu, “Robust flux estimation method for linear induction motors based on improved extended state observers,” *IEEE Trans. Power Electron.*, vol. 34, no. 5, pp. 4628–4640, May 2019, doi: 10.1109/TPEL.2018.2865800.

[19] M. Tian, B. Wang, Y. Yu, Q. Dong, and D. Xu, “Adaptive active disturbance rejection control for uncertain current ripples suppression of PMSM drives,” *IEEE Trans. Ind. Electron.*, vol. 71, no. 3, pp. 2320–2331, Mar. 2024, doi: 10.1109/TIE.2023.3265045.

[20] F. Yang et al., “Complex coefficient active disturbance rejection controller for current harmonics suppression of IPMSM drives,” *IEEE Trans. Power Electron.*, vol. 37, no. 9, pp. 10443–10454, Sep. 2022, doi: 10.1109/TPEL.2022.3168367.

[21] X. Yang, H. Hu, H. Hu, Y. Liu, and Z. He, “A quasi-resonant extended state observer-based predictive current control strategy for three-phase PWM rectifier,” *IEEE Trans. Ind. Electron.*, vol. 69, no. 12, pp. 13910–13917, Dec. 2022, doi: 10.1109/TIE.2021.3137441.

[22] S. Chen, W. Ding, R. Hu, X. Wu, and S. Shi, “Sensorless control of PMSM drives using reduced order quasi resonant-based ESO and Newton–Raphson method-based PLL,” *IEEE Trans. Power Electron.*, vol. 38, no. 1, pp. 229–244, Jan. 2023, doi: 10.1109/TPEL.2022.3199773.

[23] Y. Zuo et al., “Active disturbance rejection controller for smooth speed control of electric drives using adaptive generalized integrator extended state observer,” *IEEE Trans. Power Electron.*, vol. 38, no. 4, pp. 4323–4334, Apr. 2023, doi: 10.1109/TPEL.2022.3226160.

[24] K. Yu, Z. Wang, X. Wang, and Z. Zou, “An online flux estimation for dual three-phase SPMSM drives using position-offset injection,” *IEEE Trans. Power Electron.*, vol. 36, no. 10, pp. 11606–11617, Oct. 2021, doi: 10.1109/TPEL.2021.3067669.

[25] W. Huang, W. Hua, F. Yin, F. Yu, and J. Qi, “Model predictive thrust force control of a linear flux-switching permanent magnet machine with voltage vectors selection and synthesis,” *IEEE Trans. Ind. Electron.*, vol. 66, no. 6, pp. 4956–4967, Jun. 2019, doi: 10.1109/TIE.2018.2835381.

[26] G. Liu, B. Chen, K. Wang, and X. Song, “Selective current harmonic suppression for high-speed PMSM based on high-precision harmonic detection method,” *IEEE Trans. Ind. Informat.*, vol. 15, no. 6, pp. 3457–3468, Jun. 2019, doi: 10.1109/TII.2018.2873652.

[27] Q. Liu, L. Zhang, and W. Zhang, “High-order generalized integrator ESO-based PLL considering time-varying disturbances,” *IEEE Trans. Power Electron.*, vol. 39, no. 1, pp. 101–105, Jan. 2024, doi: 10.1109/TPEL.2023.3328647.

[28] J. Wang, K. Hu, Y. Bo, F. Wang, and J. Rodríguez, “Position sensorless control strategy based on an enhanced high order generalized integrator flux observer for PMSM drives,” *IEEE Trans. Power Electron.*, vol. 39, no. 10, pp. 12910–12924, Oct. 2024, doi: 10.1109/TPEL.2024.3425451.

Shaofeng Jia (Senior Member, IEEE) was born in Shaanxi, China. He received the B.Eng. degree in electrical engineering from Xi’an Jiaotong University, Xi’an, China, in 2012, and Ph.D. degree in electrical engineering from Huazhong University of Science and Technology, Wuhan, China, in 2017.

He is currently an Associate Professor with the School of Electrical Engineering, Xi’an Jiaotong University. He is the author/co-author of about 100 IEEE technical papers. His research interests include design and control of novel PM and reluctance machines.

Dongxu Yang (Student Member, IEEE) was born in Hebei, China. He received the B.Eng. degree in electrical engineering from Central South University, Changsha, China, in 2021. He is currently working toward the Ph.D degree in electrical engineering with Xi’an Jiaotong University, Xi’an, China.

His research interests include control and drive of permanent magnet machines.

Pengcheng Sun (Student Member, IEEE) was born in Henan, China. He received the B.Eng. degree in electrical engineering from Xi’an Jiaotong University, China, in 2019. He is currently working toward the Ph.D. degree in electrical engineering in Xi’an Jiaotong University, Xi’an, China.

His research interests include design of permanent magnet and reluctance machines.

Deliang Liang (Senior Member, IEEE) received the B.S., M.S., and Ph.D. degrees in electrical engineering from Xi’an Jiaotong University, Xi’an, China, in 1989, 1992, and 1996, respectively.

Since 1999, he has been with the School of Electrical Engineering, Xi’an Jiaotong University, where he is currently a Top Professor. From 2001 to 2002, he was a Visiting Scholar with the Science Solution International Laboratory, Tokyo, Japan. His research fields include optimal design, control, and simulation of electrical machines and electrical machine technology in renewable energy.

Jikai Si (Member, IEEE) received the B.S. degree in electrical engineering and automation from the Jiaozuo Institute of Technology, Jiaozuo, China, in 1998, the M.S. degree in electrical engineering from Henan Polytechnic University, Jiaozuo, China, in 2005, and the Ph.D. degree in electrical engineering from the China University of Mining and Technology, Xuzhou, China, in 2008.

He is currently a Distinguished Professor with Zhengzhou University, Zhengzhou, China. His main research interests include the theory and control of special motors.